Journal of Materials Chemistry

Dynamic Article Links

Cite this: J. Mater. Chem., 2012, 22, 5656

www.rsc.org/materials

PAPER

# $Co_3O_4/Ni(OH)_2$ composite mesoporous nanosheet networks as a promising electrode for supercapacitor applications†

**Jin-Hui Zhong, An-Liang Wang, Gao-Ren Li,* Jian-Wei Wang, Yan-Nan Ou and Ye-Xiang Tong**

*Received 14th November 2011, Accepted 10th January 2012*
**DOI: 10.1039/c2jm15863a**

$Co_3O_4/Ni(OH)_2$ composite mesoporous nanosheet networks (NNs) grown on conductive substrates were synthesized by heat treatment of $Co(OH)_2/Ni(OH)_2$ NNs that were synthesized on Ti substrates by a facile electrochemical deposition route. The prepared samples were characterized by X-ray diffraction (XRD), scanning electron microscopy (SEM), transmission electron microscopy (TEM), X-ray photoelectron spectroscopy (XPS), Fourier transform infrared spectroscopy (FT-IR), and micro-Raman spectroscopy. The above products were directly functionalized as supercapacitor electrodes without using any ancillary materials such as carbon black or binder. $Co_3O_4/Ni(OH)_2$ composite mesoporous NNs achieved a high specific capacitance ($C_{sp}$) of 1144 F $g^{-1}$ at 5 mV $s^{-1}$ and long-term cyclability. The electrochemical measurements showed $Co_3O_4/Ni(OH)_2$ composite mesoporous NNs exhibited much better electrochemical performances than single $Co_3O_4$ or $Ni(OH)_2$. The binary redox couples of $Ni^{2+}/Ni^{3+}$ and $Co^{2+}/Co^{3+}$, nanosheet networks with porous structures, the mesoporous structure within nanosheets, the interconnections among nanosheets, together with the excellent electrical contact with the current collector (substrate) are responsible for the improved electrochemical performances of $Co_3O_4/Ni(OH)_2$ composite mesoporous NNs. With the ease of large scale fabrication and superior electrochemical characteristics, $Co_3O_4/Ni(OH)_2$ composite mesoporous NNs grown on Ti substrates will be good candidates for supercapacitor applications.

## 1. Introduction

Supercapacitors, offering higher power density than secondary batteries and higher energy density than conventional capacitors, are attracting great attention due to not only the increasing demands for electrical devices, but also the worsening energy depletion and global warming issues.[1–4] Among various supercapacitor electrode materials, transition metal oxides offering rich redox reactions are a class of ideal materials that have drawn intense interest recently.[5–8] To date, it is well established that ruthenium oxide is a prominent material exhibiting both remarkably high specific capacitance ($C_{sp}$) and excellent reversibility.[9] However, it is not widely used owing to its high cost, the rarity of Ru, and the toxic nature of $RuO_2$. Therefore, the search for alternative cheap and environmentally friendly metal oxide materials is of significant importance for the development of supercapacitors.

Cobalt and/or nickel oxides, being cost-effective and environmentally benign, are a kind of promising materials that have wide applications in supercapacitors,[10] lithium-ion batteries,[11] magnetic devices,[12] electrocatalysts,[13] and gas sensors.[14] Recently, composite nanomaterials have attracted much interest because of their enhanced characteristics over the single material.[15] For instance, the substitution of cobalt compounds into nickel systems can contribute to the increase of electronic conductivity because the effect of d-electrons of Ni(II) and CoOOH can serve as a good current collector.[16] In contrast, Ni doping can enhance the electrochemical performance of $Co_3O_4$ by improving the active site density, conductivity, and roughness.[13] Moreover, it was also observed that the double metal oxide CoO–NiO can inherit the advantages of both cobalt and nickel oxides and has superiority over either of the single oxides in chemical-looping combustion.[17] These reports provide effective evidence about the enhancement of the composite materials over single ones. Based on the above observations, it is reasonably deducible that cobalt and nickel oxide composites possibly can result in better electrochemical characteristics, such as high $C_{sp}$ value and good electrochemical stability, than those of individual ones owing to the co-contribution of $Ni^{2+}/Ni^{3+}$ and $Co^{2+}/Co^{3+}$ redox couples, and possibly are cost-effective and environment-friendly electrode materials.

It is well accepted that, in the supercapacitor field, the ion transfer and electron conduction are the main factors that determine the electrochemical performance.[18] At present, much interest has been focused on the preparation of nanostructured electrode materials to further enhance their electrochemical properties. For example, nanorods,[19] nanowires,[20] nanotubes,[7c,21] nanosheets,[22]

*KLGHEI of Environment and Energy Chemistry, MOE Laboratory of Bioinorganic and Synthetic Chemistry, School of Chemistry and Chemical Engineering, Institute of Optoelectronic and Functional Composite Materials, Sun Yat-sen University, Guangzhou, 510275, China. E-mail: ligaoren@mail.sysu.edu.cn*

† Electronic supplementary information (ESI) available. See DOI: 10.1039/c2jm15863a

and porous/mesoporous nanostructures[23] have been widely studied for supercapacitor applications. The nanostructured electrodes with large specific surface area and porous configuration can greatly improve the electrode/electrolyte contact area, shorten the diffusion path of current carriers, and enhance the electron conduction in electrodes. Recently, the advances in the nanostructured electrodes have evoked a challenge searching for advanced nanomaterials with nanosheet network structures that will largely enhance electron conduction and with mesoporous structures that will facilitate ion transfer for enhancement of electrochemical performance of supercapacitors.[18b,24] Up to now, scientists have paid considerable efforts to synthesize novel nanostructures of cobalt oxides and nickel oxides for various applications.[25] However, cobalt and nickel oxide composite nanomaterials gain less attention, especially for supercapacitor applications.[6c] The development of facile, mild, and effective methods to synthesize cobalt and nickel oxide composite electrodes with novel nanostructures, especially network nanostructures and mesoporous structures, is still an on-going challenge. Approaching this purpose, researchers have demonstrated that electrochemical deposition is an effective and template-free way to synthesise nanostructured cobalt and nickel materials.[26]

Conventional strategies for the fabrication of electrodes are related to mixing and pressing powder of active material with ancillary materials such as carbon black or binder to enhance the conductivity and solidity of the system since the material is not directly grown on conductive substrates. Moreover, besides the lengthy fabrication procedures, the conventional methods also lead to a compact structure which is unfavorable for fast electron transfer and electrolyte diffusion.[27,28] However, the nanomaterials grown on conductive substrates can be directly utilized as electrodes for electrochemical devices involving no ancillary materials or lengthy procedures. More importantly, each self-supported nanostructure, such as nanowire and nanosheet, grown on a conductive substrate can participate in the reaction effectively because of its excellent electrical contact to the substrate, *i.e.*, the current collector.[13,29–31]

In light of the above considerations, novel $Co_3O_4/Ni(OH)_2$ composite mesoporous nanosheet networks (NNs) were synthesized on a conductive substrate for supercapacitor application by heat treatment of $Co(OH)_2/Ni(OH)_2$ NNs grown on a Ti substrate *via* a facile electrochemical route. The prepared $Co_3O_4/Ni(OH)_2$ composite mesoporous NNs on the conductive substrate simultaneously possess binary redox couples of $Ni^{2+}/Ni^{3+}$ and $Co^{2+}/Co^{3+}$, large specific surface area, continuous nanosheet networks, porous/mesoporous nanostructures, and excellent electrical contact with the current collector (substrate). The electrochemical measurements demonstrated $Co_3O_4/Ni(OH)_2$ composite mesoporous NNs grown on conductive substrates exhibited high supercapacitive performances and long-term cyclability, indicating potential applications as high-performance supercapacitor electrode materials.

## 2. Experimental section

### Synthesis of $Co(OH)_2/Ni(OH)_2$

All electrochemical deposition experiments were performed with a HDV-7C transistor potentiostatic apparatus that was connected with a simple three-electrode cell. The graphite electrode was used as a counter electrode (spectral grade, 2.0 $cm^2$). The saturated calomel electrode (SCE) was used as the reference electrode that was connected to the cell with a double salt bridge system. The Ti plates (99.9 wt%) were used as the working electrode, and they were prepared *via* the following steps before each experiment: firstly polished by SiC abrasive paper from 300 to 800 grits, then dipped in HCl solution (0.1 M) for 5 min and rinsed with acetone in an ultrasonic bath for 5 min, and finally washed with distilled water. $Co(OH)_2/Ni(OH)_2$ composites were cathodically electrodeposited on the Ti substrate in a solution of 0.01 M $Ni(NO_3)_2$ + 0.02 M $Co(NO_3)_2$ + 0.2 M $NH_4Cl$ (here $NH_4Cl$ was used as additive) by galvanostatic electrolysis with a current density of 1.0 mA $cm^{-2}$ for 90 min at 70 °C.

### Synthesis of $Co_3O_4/Ni(OH)_2$

The as-prepared $Co(OH)_2/Ni(OH)_2$ composites were placed in a crucible that was put into the center of a quartz tube and heated in a horizontal furnace. The heat treatment of the prepared $Co(OH)_2/Ni(OH)_2$ composites was performed under air atmosphere at 200, 300, and 400 °C for 12 h, respectively. The $Co_3O_4/Ni(OH)_2$ composite mesoporous NNs were synthesized by heat treatment of $Co(OH)_2/Ni(OH)_2$ composite NNs at 200 °C for 12 h.

### Sample characterization

The surface morphologies of the products were characterized using a field emission scanning electron microscope (SEM, FEI, Quanta 400). A transmission electron microscope (TEM, JEM-2010HR), high-resolution TEM (HRTEM, 200 kV), and electron diffraction (ED) were also utilized to characterize the microstructures of the products. The obtained products were also analyzed by X-ray diffraction (XRD, Bruker, D8 Advance) to determine the film structures. X-ray energy dispersive spectroscopy (EDS), X-ray photoelectron spectroscopy (XPS, ESCALAB 250), Fourier transform infrared spectroscopy (FTIR, Nicolet 330), and laser micro-Raman spectroscopy (Renishaw inVia) were applied to study the chemical compositions and structures of the products. The thermal behavior of the deposits was analyzed by thermal gravimetric (TG) analysis (TG-209, Netzsch), measured from 20 to 700 °C at a heating rate of 10 °C $min^{-1}$ in air. The samples were also characterized by Brunauer, Emmett, and Teller (BET) nitrogen sorption surface area measurements (Micromeritics ASAP 2010). Specific surface areas of the products were calculated by the BET method, and pore sizes were calculated using the Barrett, Joyner, and Halenda (BJH) method (for large pores) or the density functional theory (DFT) method (for small pores) on the basis of the desorption branch of the nitrogen sorption isotherms. The electrochemical measurements were carried out in a Chi660C electrochemical workstation. The prepared $Co(OH)_2/Ni(OH)_2$ and $Co_3O_4/Ni(OH)_2$ composites with 0.5 mg $cm^{-2}$ on a Ti substrate were directly used as electrodes for redox supercapacitor applications in a solution of 1.0 M NaOH. The platinum sheet was used as the counter electrode. The Ag/AgCl electrode was used as the reference electrode that was connected to the cell with a double salt bridge system. The cyclic voltammetry (CV) experiments

were performed between 0.04 and 0.52 V at a scan rate of 5–100 mV $s^{-1}$. The galvanostatic charge–discharge (CD) behavior was investigated within the potential window 0–0.5 V at 1.0 mA $cm^{-2}$. All potentials in this study were the values *versus* the reference electrode.

## 3. Results and discussion

The electrodeposition of $Co(OH)_2/Ni(OH)_2$ composites was firstly carried out in a solution of 0.01 M $Ni(NO_3)_2$ + 0.02 M $Co(NO_3)_2$ + 0.2 M $NH_4Cl$ with a current density of 1.0 mA $cm^{-2}$ for 90 min at 70 °C. The as-prepared composites with green color were distributed uniformly and adhered firmly onto the Ti substrate (Fig. 1a). SEM images of the deposits with different magnifications are shown in Fig. 1c and d, and they clearly show $Co(OH)_2/Ni(OH)_2$ composites have nanosheet networks (NNs) with porous structures. The large amount of open space among NNs will be beneficial for the diffusion of electroactive species, leading to reduced internal resistance.[13] The thicknesses of nanosheets are about 20–25 nm. Interestingly, these nanosheets are connected with each other to form the network structures, as marked in the white rectangular dashed boxes in Fig. 1c (inset) and 1d, which will favor the electron transportation among the whole NN area. TEM and HRTEM images of as-prepared $Co(OH)_2/Ni(OH)_2$ composite nanosheets are shown in Fig. 1e and f, respectively. It can be clearly observed that the product has a sheet-like morphology, which is consistent with SEM observation. The HRTEM image clearly shows that the lattice fringes derive from the same crystalline grains. The lattice spacing is estimated to be about 2.69 Å, which corresponds to the (100) planar space of α-$Co(OH)_2$. So the crystal growth of the nanosheets is preferential in the [100] direction. The corresponding SAED pattern shown in the inset in Fig. 1f displays hexagonally arranged diffraction spots, and it also shows that the prepared α-$Co(OH)_2$ nanosheet consists of single crystal structures with preferential growth in the [100] direction. However, no information associated with $Ni(OH)_2$ is detected in HRTEM and SAED analyses, indicating $Ni^{2+}$ ions possibly have been uniformly doped into α-$Co(OH)_2$ lattices.[32]

XRD measurement was carried out to determine the phases of the as-prepared $Co(OH)_2/Ni(OH)_2$ composites. Fig. 1b shows the typical XRD pattern of the products. Three diffraction peaks at 7.98, 4.00 and 2.64 Å in the XRD pattern can be assigned to the 003, 006, and 009 reflections of the hydrotalcite-like structure (unit cell with three slabs),[33–35] noting that $d_{003} \approx 2d_{006} \approx 3d_{009}$. Taking account of its green color, the above three diffractions can be attributed to α-$Co(OH)_2$.[33–36] However, no relational Ni crystalline forms including $Ni(OH)_2$ are detected. This is accordant with the above results of HRTEM and SAED. In addition, it should be noted that XRD peaks of α-$Co(OH)_2$ in the $2\theta$ range from 10° to 70° exhibit a little shift toward larger angles because of the incorporation of Ni. Since the ionic radius of $Ni^{2+}$ (69 pm) ion is smaller than that of $Co^{2+}$ ion (79 pm), the lattice of $Co(OH)_2$ will constrict upon Ni doping. This lattice shrinkage will lead to the positive shift of α-$Co(OH)_2$ peaks. No other impurities are detected besides the reflections from the Ti substrate, indicating high purity of the prepared $Co(OH)_2/Ni(OH)_2$ composites. The EDS pattern in Fig. 1g reveals that the as-prepared deposits contain Co, Ni, O, Ti and Cl elements. The elements Co, Ni, and O come from $Co(OH)_2/Ni(OH)_2$ composites. The signals of Ti come from the substrate, and Cl signals are due to $Cl^-$ anions adsorbed in deposits. The EDS results show the ratio of Co/Ni is about 2, suggesting the ratio of $Co(OH)_2/Ni(OH)_2$ is 2. The XPS and FTIR spectra shown in Fig. S1† further demonstrate the existence of α-$Co(OH)_2$ and $Ni(OH)_2$ in deposits.

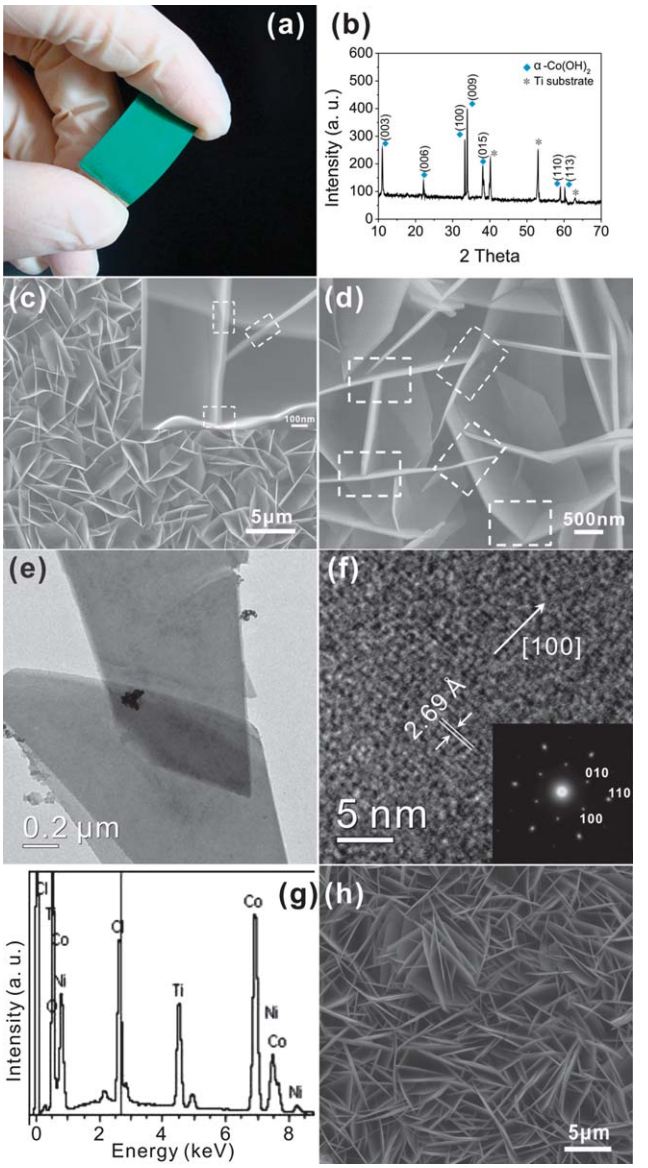


**Fig. 1** The chemical and structural characterization of $Co(OH)_2/Ni(OH)_2$ NNs prepared with $NH_4Cl$ concentration of 0.2 M: (a) optical image, (b) XRD pattern, (c–d) SEM images, (e) TEM image, (f) HRTEM image and the corresponding SAED pattern (inset), and (g) EDS spectrum. (h) Typical SEM image of $Co(OH)_2/Ni(OH)_2$ composite prepared with $NH_4Cl$ concentration of 0.02 M.

The electrochemical formation process of $Co(OH)_2/Ni(OH)_2$ composites during electrodeposition is explained as follows. The electro-reduction of nitrate ions ($NO_3^-$ to $NO_2^-$) *via* reaction (1),[37,38] and further reduction from $NO_2^-$ to $N_2$ *via* reaction (2),[39,40] can produce $OH^-$ ions which gives rise to the formation of $Ni(OH)_2$ and $Co(OH)_2$ *via* reactions (3) and (4), respectively.

And accordingly $Co(OH)_2/Ni(OH)_2$ composites are formed. Before electrodeposition, in the solution of 0.01 M $Ni(NO_3)_2$ + 0.02 M $Co(NO_3)_2$ + 0.2 M $NH_4Cl$, the bivalent $M^{2+}$ (M = Co, Ni) ions will be fully coordinated with $NH_4^+$ ions that come from $NH_4Cl$ (0.2 M) to form $M(NH_3)_x^{2+}$ ions.[41] Therefore, during electrodeposition, the number of nucleation center is limited and the growth rates of $Co(OH)_2$ and $Ni(OH)_2$ are slow because of the existence of $M(NH_3)_x^{2+}$ ions, leading to the formation of ordered structures. These nanosheets connect with each other and form network structures. In addition, the larger number of nucleation centers and the faster growth rate of the deposits, as a result of the lower concentration of $NH_4Cl$ (0.02 M), will lead to the denser structures as shown in Fig. 1h.

$$NO_3^- + H_2O + 2e \rightarrow NO_2^- + 2OH^- \quad (1)$$

$$2NO_2^- + 4H_2O + 6e \rightarrow N_2 + 8OH^- \quad (2)$$

$$Ni^{2+} + 2OH^- \rightarrow Ni(OH)_2 \quad (3)$$

$$Co^{2+} + 2OH^- \rightarrow Co(OH)_2 \quad (4)$$

The electrochemical performances of the as-prepared $Co(OH)_2/Ni(OH)_2$ NNs were investigated by CV and galvanostatic CD tests, which are effective tools to present the capacitive behavior of a electrode material. $C_{sp}$ values can be calculated from CV curves by means of $C_{sp} = i/m(dV/dt)$, where $i$ is the average current in the capacitive potential region, $dV/dt$ is the scan rate, and $m$ is the mass of material,[42] or from CD curves by $C_{sp} = C/m = It/Vm$, where $I$ is the charge–discharge current, $t$ is the discharge time, $V$ is the electrochemical window, and $m$ is the mass of active material,[43] here the specific mass loading of the material is 0.5 mg $cm^{-2}$. Based on the CV curve measured at 5 mV $s^{-1}$ in a solution of 1.0 M NaOH as shown in Fig. 2a, the as-prepared $Co(OH)_2/Ni(OH)_2$ NNs achieve a high $C_{sp}$ value of 823 F $g^{-1}$, which is larger than 710 F $g^{-1}$ of the disordered nanosheets. Fig. 2b represents the charge–discharge curves of $Co(OH)_2/Ni(OH)_2$ NNs and disorder nanosheets within 0–0.5 V at a current density of 1.0 mA $cm^{-2}$, and it also shows $Co(OH)_2/Ni(OH)_2$ NNs have better electrochemical performances than the disordered nanosheets. The binary redox couples of $Ni^{2+}/Ni^{3+}$ and $Co^{2+}/Co^{3+}$, interconnections among nanosheets, nanosheet networks with porous structures, together with the excellent electrical contact with the substrate were responsible for the high $C_{sp}$ of $Co(OH)_2/Ni(OH)_2$ NNs. Based on the specific capacitance performance depending on the thickness of the electrode material, the dependence of specific capacitance on the specific mass loading of the as-prepared $Co(OH)_2/Ni(OH)_2$ NNs was also investigated at 5 mV $s^{-1}$. The CV curves and the specific capacitance as a function of the specific mass loading are shown in Fig. S2,† which suggests that the specific capacitance reaches a maximum value of 823 F $g^{-1}$ at 0.5 mg $cm^{-2}$. When the loading is larger than 0.5 mg $cm^{-2}$, the overgrowth may result in blockage of the porous structure which is responsible for the decrease of specific capacitance.[42] However, $Co(OH)_2/Ni(OH)_2$ NNs do not show good cyclability according to the cycle-life data as shown in Fig. 2c. After 500 cycles, the $C_{sp}$ of $Co(OH)_2/Ni(OH)_2$ NNs is decreased from 823 to 520 F $g^{-1}$. The fact is that $\alpha$-$Co(OH)_2$ is metastable and will be easily transformed to $\beta$-$Co(OH)_2$ in strong alkaline media.[44] The rapid decrease of $C_{sp}$ in the first 200 cycles may be due to the transformation of $\alpha$-$Co(OH)_2$ $\rightarrow$ $\beta$-$Co(OH)_2$ during cycle tests because $\beta$-$Co(OH)_2$ theoretically possesses poor electrochemical performance compared with $\alpha$-$Co(OH)_2$.[45]

Although $Co(OH)_2/Ni(OH)_2$ NNs with loading of 0.5 mg $cm^{-2}$ show high $C_{sp}$ of 823 F $g^{-1}$ at 5 mV $s^{-1}$, their poor cyclability cannot meet the requirement of high-performance supercapacitors. In order to achieve better electrochemical performances (*e.g.*, better cyclability), here heat treatment of $Co(OH)_2/Ni(OH)_2$ NNs was carried out under air atmosphere at 200, 300 and 400 °C for 12 h, and accordingly the heat-treated samples are named as NiCoO-200, NiCoO-300 and NiCoO-400 NNs, respectively. SEM images of $Co(OH)_2/Ni(OH)_2$ NNs calcined at different temperatures are shown in Fig. 3, which shows the surface morphologies of these samples experience little change and maintain their nanosheet network structure integrity after calcination at 200, 300 and 400 °C. Moreover, the interconnection nature in the structure of NNs is also observed in SEM images.

TG and its differential (DTG) curves of as-prepared $Co(OH)_2/Ni(OH)_2$ NNs in the temperature range of 20–700 °C are shown in Fig. 4. The sample underwent a weight loss of 23.98% in four steps indicated by the zones I, II, III, and IV on the graph. The weight loss (6.34%) below 160 °C (domain I) is assigned to the removal of the adsorbed water and the evaporation of the intercalated water molecules. The decomposition of $\alpha$-$Co(OH)_2$ begins at 160 °C while $\beta$-$Ni(OH)_2$ does not decompose until 215 °C as shown in DTG data. The weight loss (12.0%) between 160 and 370 °C is associated with the loss of water produced by the decomposition and dehydroxylation of $Co(OH)_2$ and $Ni(OH)_2$. Finally, the fourth domain ending at 600 °C can be ascribed to the loss of $Cl^-$ ions adsorbed from the deposition solution. These results are consistent with the previous reports of $Co(OH)_2$ and $Ni(OH)_2$.[46,47]

XRD patterns of the samples calcined at different temperatures are shown in Fig. 5a. For sample NiCoO-200 NNs, the

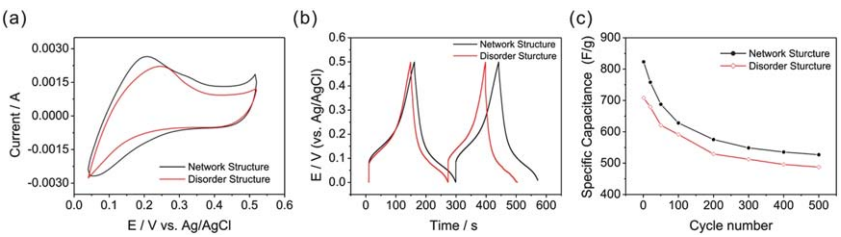


**Fig. 2** CV curves (a), charge–discharge behavior (b) and cycle-life data (c) of as-prepared $Co(OH)_2/Ni(OH)_2$ composites with nanosheet network structure (black curve) and nanosheet disordered structure (red curve). The specific mass loading is 0.5 mg $cm^{-2}$.

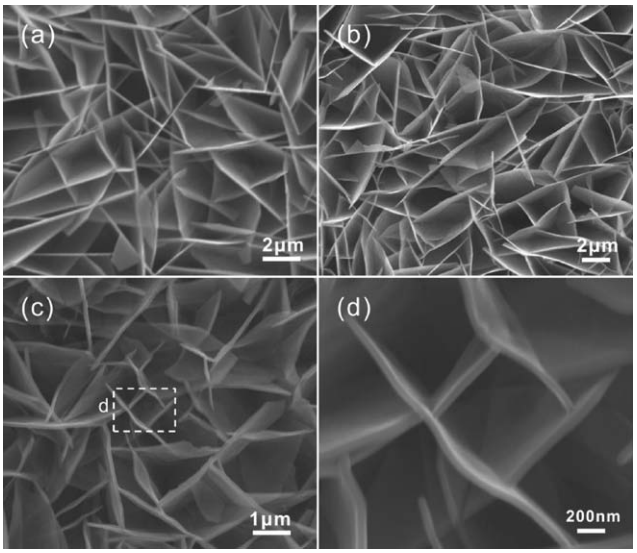


**Fig. 3** SEM images of the products calcined at (a) 200 °C (NiCoO-200), (b) 300 °C (NiCoO-300) and (c, d) 400 °C (NiCoO-400).

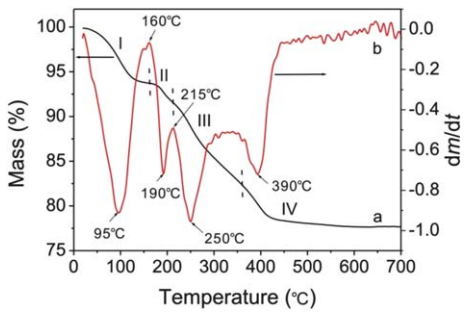


**Fig. 4** TG (a) and DTG (b) curves of as-prepared $Co(OH)_2/Ni(OH)_2$ composites.

relatively broad peak located at $2\theta = 36.8°$ can be indexed to the (311) plane of $Co_3O_4$ (JCPDS 42-1467), and other peaks come from the substrate. Since $Ni(OH)_2$ does not decompose before 200 °C as shown in Fig. 4, the composition of sample NiCoO-200 NNs should be $Co_3O_4$ and $Ni(OH)_2$. No $Ni(OH)_2$ peak is observed in the XRD pattern, indicating $Ni^{2+}$ ions possibly have been uniformly doped into $Co_3O_4$ lattices. Besides the peaks of substrate, the peaks of samples NiCoO-300 and NiCoO-400 NNs can be indexed to $NiCo_2O_4$ (JCPDS 20-0781) as shown in Fig. 5a, indicating $Co(OH)_2$ and $Ni(OH)_2$ both have been decomposed at 300 and 400 °C because the elements Co and Ni in $NiCo_2O_4$ only come from $Co(OH)_2$ and $Ni(OH)_2$. In addition, the peaks of NiCoO-200, NiCoO-300 and NiCoO-400 NNs are broad, implying the nanocrystalline nature in these materials.[48] With increasing calcination temperature, the peaks of samples turn relatively narrow, indicating the growth of the grain size. The mean grain sizes of NiCoO-200, NiCoO-300 and NiCoO-400 NNs are estimated by the Scherrer equation using the (311) peak in each sample, and they are approximately 9.6, 16.7 and 20.1 nm, respectively.

XPS analyses provide a careful study of the compositions of the samples calcined at different temperatures, and the results are shown in Fig. 5 (b–d). In NiCoO-200 NNs data in Fig. 5b, the

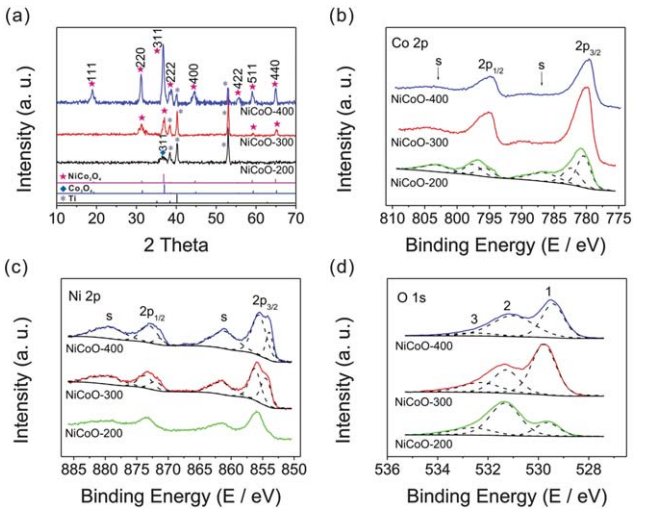


**Fig. 5** XRD patterns (a) and XPS spectra of (b) Co 2p, (c) Ni 2p and (d) O 1s of the products calcined at 200 °C, 300 °C, and 400 °C (from bottom to top), respectively.

binding energy at 780.3 eV ascribed to $Co^{3+}$ in octahedral sites, the binding energy at 782.2 eV and the satellite structure ascribed to $Co^{2+}$ in tetrahedral sites, are clearly evident in the cobalt 2p spectra.[49–51] In NiCoO-200 NNs data in Fig. 5c, the nickel $2p_{3/2}$ binding energy at 856.0 eV and the much intense satellite peak are characteristics of $Ni^{2+}$ in $Ni(OH)_2$,[52–54] which also suggests that no decomposition occurs at 200 °C from $Ni(OH)_2$ to nickel oxide since the latter should give a lower binding energy value at ~854 eV.[53] In NiCoO-200 NNs data in Fig. 5d, the first peak of O 1s spectra at 529.7 eV is due to the contribution of $O^{2-}$ in rocksalt and spinel metal oxides, such as $Co_3O_4$.[55] The assignment of the second O 1s peak at 531.3 eV is somewhat complicated. Kim and co-workers summarized that this peak can be assigned to defects, contaminants, and a number of surface species including hydroxyls, chemisorbed oxygen, under-coordinated lattice oxygen, $Ni_2O_3/Co_2O_3$-like surface phases, or species intrinsic to the surface of the spinel.[50] Despite many possible assignments, the intensity of the peak at 531.3 eV is generally about 30–40% of that of the peak at 529.7 eV in rocksalt and spinel metal oxides.[50] However, for the O 1s XPS spectrum of NiCoO-200 NNs, the intensity of the peak at 531.3 eV is about 2.5 times that of the peak at 529.7 eV, which indicates the partial contribution of O in $OH^-$ species in $Ni(OH)_2$ cannot be excluded.[56] The third peak of O 1s at about 532.5 eV can be assigned to oxygen species in surface-absorbed water molecules.[51] The XPS results, consistent with TG and XRD results, further confirm the composition is $Co_3O_4/Ni(OH)_2$ for NiCoO-200 NNs.

The XPS spectra of elements Co, Ni and O in NiCoO-300 and NiCoO-400 NNs are almost the same as shown in Fig. 5(b–d). With the calcination temperature further increasing to 300 °C and 400 °C, $Ni(OH)_2$ decomposes and then reacts with $Co_3O_4$ to form $NiCo_2O_4$. The binding energies at 780.0 and 795.2 eV for $2p_{3/2}$ and $2p_{1/2}$ transitions are associated with $Co^{3+}$. The relatively narrow peak width, the $2p_{3/2}$ to $2p_{1/2}$ separation of 15.2 eV, and the absence of any shake-up peak all reveal that no $Co^{2+}$ cations exist in $NiCo_2O_4$.[49,50] The nickel $2p_{3/2}$ spectra can be assigned to two distinct peaks, indicating the presence of both $Ni^{2+}$ and

 

$Ni^{3+}$.[36,53] The O 1s spectra at binding energies of 529.6 and 531.2 eV are ascribed to $O^{2-}$ species in $NiCo_2O_4$.[49,50] The formula of $NiCo_2O_4$ can be generally expressed as follows: $Co^{2+}_{1-x}Co^{3+}_x[Co^{3+}Ni^{2+}_xNi^{3+}_{1-x}]O_4$ ($0 \leq x \leq 1$) (the cations within brackets are in octahedral sites and the outside ones are in tetrahedral sites).[50] Therefore, based on the above XPS results, here the formula of NiCoO-300 and NiCoO-400 NNs can be expressed as $Co^{3+}[Co^{3+}Ni^{2+}_xNi^{3+}_{1-x}]O_4$ because of the absence of $Co^{2+}$ ions.

Raman spectra shown in Fig. 6f provide additional evidence for the overall conversion process during calcination. With respect to the as-prepared $Co(OH)_2/Ni(OH)_2$ NNs, the peaks at 250, 437, 515, 3500, and 3620 $cm^{-1}$ correspond to $E_g$, $E_u$, $A_{2u}$, $A_{1g}$, and $A_{2u}$ models of $Co(OH)_2$ and $Ni(OH)_2$, respectively. For sample NiCoO-200, $A_{1g}$ (3560 $cm^{-1}$) symmetric stretching internal hydroxyl model of $Ni(OH)_2$ is observed. Another four peaks at 186, 480, 520, and 670 $cm^{-1}$ corresponding to $F_{2g}$, $E_g$, $F_{2g}$, $A_{1g}$ models of $Co_3O_4$, respectively, are also examined. So the above results show the sample NiCoO-200 NNs are composed of $Co_3O_4/Ni(OH)_2$. Raman signals of NiCoO-300 and NiCoO-400 NNs are similar to each other as shown in Fig. 6f. Besides the $F_{2g}$ (180 $cm^{-1}$) model, a board band at 400–700 $cm^{-1}$ corresponding to Co–O and Ni–O vibrations is detected for samples NiCoO-300 and NiCoO-400 NNs, and no signal corresponding to OH groups is observed, indicating $Co(OH)_2$ and $Ni(OH)_2$ are completely decomposed after 300 °C. These results were consistent with those documented in previous reports.[57–59] The above Raman spectra further confirm the phase transformation from $Co(OH)_2/Ni(OH)_2$ to $Co_3O_4/Ni(OH)_2$ (NiCoO-200) and finally $NiCo_2O_4$ (NiCoO-300, NiCoO-400) with calcination temperature increasing.

TEM images of NiCoO-200, NiCoO-300, and NiCoO-400 NNs are shown in Fig. 6. When the calcination was carried out at 200 °C, the as-prepared composites underwent a number of physical and chemical processes. The removal of water in the structure, including the adsorbed, intercalated and hydroxyl water, opens up pore spaces and results in the formation of mesoporous structures in nanosheets, which are clearly observed in the TEM image of sample NiCoO-200 NNs as shown in Fig. 6a. As we all know, the mesoporous structures in nanosheets will greatly improve the electrode/electrolyte contact area, shorten the diffusion path of current carriers, and accordingly have huge potential to further enhance their electrochemical performances. The black pillar of about 23 nm in width in Fig. 6a (indicated by the arrow) corresponds to a nanosheet vertically connecting to the visual one lying on a Cu grid (a sketch map is shown in inset in Fig. 6a), suggesting the interconnection nature of nanosheet networks. The fringe spacing is determined to be about 2.44 Å according to the HRTEM image in Fig. 6b, which corresponds to the (311) planar spacing of $Co_3O_4$ (JCPDS 42-1467). The inset in Fig. 6b shows the corresponding SAED pattern and it shows the quasi-single-crystalline nature of $Co_3O_4$.[60] The absence of signals related to $Ni(OH)_2$ in XRD, HRTEM and SAED analyses of NiCoO-200 NNs may be attributed to the doping of $Ni^{2+}$ ions into $Co_3O_4$ lattices. The TEM and HRTEM images of NiCoO-300 NNs are shown in Fig. 6c and 6d, respectively. The lattice fringes are clearly displayed in the HRTEM image, indicating NiCoO-300 NNs is high crystallinity and single crystalline. The lattice fringe is measured about 2.45 Å from the HRTEM image, matching well with the (311) facet distance of $NiCo_2O_4$ (JCPDS 20-0781). The SAED pattern of NiCoO-300 NNs shown in the inset in Fig. 6d shows the single-crystalline nature of $NiCo_2O_4$. The mesoporous structures are also observed in the nanosheet in NiCoO-300 NNs as shown in Fig. 6c. With more close observation, the average pore size in NiCoO-300 NNs is larger than that in NiCoO-200 NNs. The mesoporous structure in the sample NiCoO-400 NNs is shown in Fig. 6e. The pore size in NiCoO-400 NNs is similar to

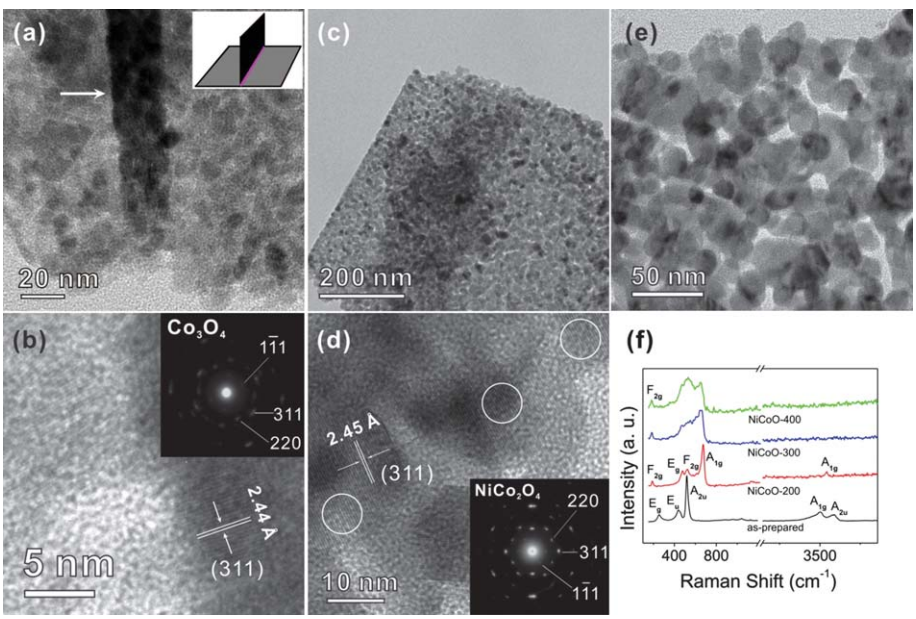


**Fig. 6** TEM images of NiCoO-200 (a, b), NiCoO-300 (c, d) and NiCoO-400 (e), the inset shows the corresponding SAED patterns, the three circles in (d) indicate NiCoO-300 has the same crystal orientation at different parts of the mesoporous structure. (f) Raman spectra of the products calcined at different temperatures.

that in NiCoO-300 NNs, suggesting the pore size in the mesoporous structure does not change after 300 °C. The mean grain sizes of the samples NiCoO-200, NiCoO-300, and NiCoO-400 NNs are estimated about 7.9, 13.7, and 17.7 nm, respectively, from the corresponding TEM images. These values of grain sizes are in good agreement with XRD results.

Fig. 7 shows $N_2$ sorption isotherms of NiCoO-200, NiCoO-300, and NiCoO-400 mesoporous NNs calcined at different temperatures. NiCoO-200 mesoporous NNs give a high BET specific surface area of about 80.3 $m^2$ $g^{-1}$ and a narrow distribution of pore size calculated from the desorption isotherm as shown in Fig. 7a (inset). The pore sizes are mainly distributed around 2.8–4.3 nm that is the optimal pore size for the diffusion of active species in electrode materials.[6c] Compared with the as-prepared $Co(OH)_2/Ni(OH)_2$ NNs with surface area of about 10.8 $m^2$ $g^{-1}$, NiCoO-200 mesoporous NNs show much larger surface area of 80.3 $m^2$ $g^{-1}$, and largely increase the electrode/electrolyte contact area for the performance enhancement. The dramatic increase of surface area of NiCoO-200 NNs may be attributed to the generation of mesoporous structures in nanosheets. However, at higher treatment temperatures, such as 300 and 400 °C, the samples will experience not only a decrease of the specific surface area, from 80.3 $m^2$ $g^{-1}$ (NiCoO-200 NNs) to 59.1 $m^2$ $g^{-1}$ (NiCoO-300 NNs) and 37.7 $m^2$ $g^{-1}$ (NiCoO-400 NNs), but also an increase of the pore size as shown in Fig. 7 (insets).

The electrochemical performances of the NiCoO-200, NiCoO-300, and NiCoO-400 mesoporous NNs were studied. The CV curve of NiCoO-200 mesoporous NNs composed of $Co_3O_4$ and $Ni(OH)_2$ is shown in Fig. 7d. The near-rectangular-shaped CV curve and the mirror image characteristics to the zero-current axis suggest the highly capacitive behavior and reversibility.[61] According to the CV test shown in Fig. 7d, NiCoO-200 mesoporous NNs exhibits a high $C_{sp}$ value of 684 F $g^{-1}$ at 5 mV $s^{-1}$, which is a little smaller than 823 F $g^{-1}$ of $Co(OH)_2/Ni(OH)_2$ NNs. This may be attributed to the conversion of $Co(OH)_2$ to

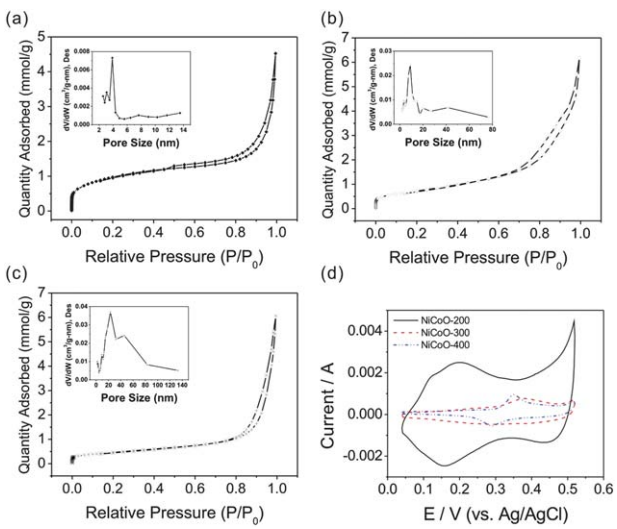


**Fig. 7** $N_2$ adsorption–desorption isotherms and corresponding pore size distribution curves (inset) of the products calcined at (a) 200 °C, (b) 300 °C and (c) 400 °C. (d) CVs of the samples calcined at different temperatures. The specific mass loading is 0.5 mg $cm^{-2}$.

$Co_3O_4$ since $Ni(OH)_2$ still exists in NiCoO-200. With calcination temperature increasing, NiCoO-300 and NiCoO-400 mesoporous NNs exhibit $C_{sp}$ values of about 282 and 136 F $g^{-1}$ at 5 mV $s^{-1}$, respectively, which are much lower than those of NiCoO-200 mesoporous NNs and $Co(OH)_2/Ni(OH)_2$ NNs. The decrease of $C_{sp}$ values of NiCoO-300 and NiCoO-400 mesoporous NNs with increasing calcination temperature can be explained as follows. (a) When the calcination temperature was increased to above 300 °C, $Co(OH)_2/Ni(OH)_2$ NNs were completely decomposed to form $NiCo_2O_4$, which has a poor supercapacitive property compared with $Co(OH)_2$ and $Co_3O_4$. (b) With increasing calcination temperature from 200 to 400 °C, the crystallinity of the products turns better according to XRD and TEM measurements, and this is unfavorable for electrolyte penetrating into the internal part of the electrode material. The relatively poor crystallinity, leading to more structural defects that can provide more diffusion channels for proton and cations, also improves the electrochemical activity.[62,63] (c) Compared with NiCoO-200 mesoporous NNs, the larger grain sizes in NiCoO-300 and NiCoO-400 mesoporous NNs result in lower proton diffusion coefficient and conductivity, since the smaller particle size would give the larger surface area and the enhanced surface hydration.[64,65] The smaller grain size in NiCoO-200 mesoporous NNs also contributes to the larger percentage of deposits exposed on the outer surface and can ensure more active sites for electrochemical reactions. (d) Compared with NiCoO-200 mesoporous NNs, the smaller specific surface areas of NiCoO-300 and NiCoO-400 mesoporous NNs account for less active sites that are crucial for redox faradaic reactions.

Based on the special mesoporous nanosheet network structures and high $C_{sp}$ value, the electrochemical cyclability of NiCoO-200 NNs was further investigated by CV measurements for 500 cycles, and the cycle-life data is shown in Fig. 8a. Interestingly, the $C_{sp}$ value of NiCoO-200 mesoporous NNs shows a rapid increase, rather than decrease, with increasing cycle number in the initial 10 cycles. After 10 cycles, the $C_{sp}$ rapidly increases to the maximum 1144 F $g^{-1}$ from the primary value of 684 F $g^{-1}$. The large enhancement of $C_{sp}$ value after 10 cycles may be attributed to the structure improvement, such as the enhancement of void ratio or specific surface area, or full activation of the product during electrochemical cycling.[6c,62,66] A decay of about 6.6% of $C_{sp}$ with respect to the maximal value is observed after 500 cycles (4.6% in the first 200 cycles and 2.0% in the subsequent 300 cycles), indicating an excellent cyclability for a long-term application. In addition, after 10 cycles, NiCoO-200 mesoporous NNs show much larger $C_{sp}$ and much higher electrochemical cyclability than those of $Co(OH)_2/Ni(OH)_2$ NNs shown in Fig. 2b, indicating an enhancement of electrochemical performances after heat-treatment at 200 °C. Fig. 8b shows the $C_{sp}$ of NiCoO-200 mesoporous NNs as a function of scan rate. A decrease in $C_{sp}$ of about 34% is observed with scan rate increasing from 5 to 100 mV $s^{-1}$, indicating a good rate capability. Therefore, NiCoO-200 mesoporous NNs show attractive performances for supercapacitor with high $C_{sp}$ and long cycle life.

A comparison of electrochemical performances of NiCoO-200 mesoporous NNs with those of single $Co_3O_4$ and $Ni(OH)_2$ was examined. The individual $Co_3O_4$ and $Ni(OH)_2$ samples with similar surface morphologies were prepared and calcined at

 

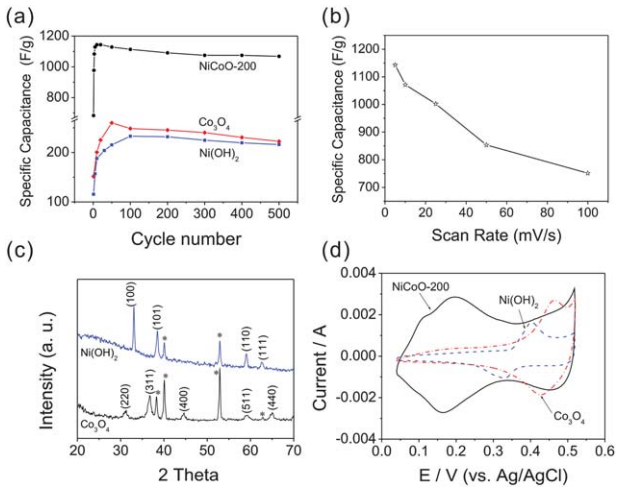


**Fig. 8** (a) Cyclability tests of samples NiCoO-200, $Ni(OH)_2$ and $Co_3O_4$. (b) Plots of $C_s$ as a function of scan rate of NiCoO-200 sample. (c) XRD patterns of $Co_3O_4$ and $Ni(OH)_2$ after calcination at 200 °C (symbol * indicates Ti substrate). (d) CV curves of samples NiCoO-200, $Ni(OH)_2$ and $Co_3O_4$. The specific mass loading is 0.5 mg $cm^{-2}$.

200 °C using similar conditions. Fig. 8c illustrates the XRD patterns of $Ni(OH)_2$ and $Co_3O_4$, and all the diffraction peaks can be well indexed to $Ni(OH)_2$ (JCPDS 14-0117) and $Co_3O_4$ (JCPDS 42-1467). CV curves of samples NiCoO-200, $Co_3O_4$ and $Ni(OH)_2$ were measured at 5 mV $s^{-1}$ in a solution of 1.0 M NaOH, and they are displayed in Fig. 8d. The CV curve of NiCoO-200 mesoporous NNs exhibits much larger enclosed area and wider distribution than those of $Ni(OH)_2$ and $Co_3O_4$. The $C_{sp}$ values of $Ni(OH)_2$ and $Co_3O_4$ are calculated about 113 and 161 F $g^{-1}$ at 5 mV $s^{-1}$, respectively, which are much lower than the value of 684 F $g^{-1}$ of NiCoO-200 mesoporous NNs. What else should be pointed out here is that the $C_{sp}$ of NiCoO-200 mesoporous NNs is also much higher than the summation of $C_{sp}$ values of $Co_3O_4$ and $Ni(OH)_2$ as shown in Fig. 8a, which suggests the improved electrochemical performances of the composites come from not only a mechanical combination but also an inter-enhancement effect of these two oxides. The achieved high $C_{sp}$ value of 1144 F $g^{-1}$ of $Co_3O_4/Ni(OH)_2$ NNs can be explained by the following merits: (a) the porous network structures that favor the diffusion of active species, (b) the mesoporous structure ensures fast proton transfer and provides a large $OH^-$ and cation accessible area, (c) the easy electron transportation among nanosheets because of the interconnections between them, (d) the binary redox couples of $Co^{2+}/Co^{3+}$ and $Ni^{2+}/Ni^{3+}$ affording rich faradaic capacitance, and (e) the enhanced conductivity due to the direct growth of the material on the current collector.

## 4. Conclusions

Herein, we synthesized $Co_3O_4/Ni(OH)_2$ (NiCoO-200) composite mesoporous NNs as an interesting electrode material with high $C_{sp}$ and long cycle life for supercapacitor applications. Firstly, large area $Co(OH)_2/Ni(OH)_2$ composite NNs were synthesized on a conductive substrate by a facile and efficient electrochemical route. Electrochemical measurements revealed that $Co(OH)_2/Ni(OH)_2$ composite NNs displayed high $C_{sp}$ but lousy cyclability. Then the $Co_3O_4/Ni(OH)_2$ composite mesoporous NNs grown on conductive substrates were prepared from $Co(OH)_2/Ni(OH)_2$ composite NNs by heat-treatment. The resulting products also have been successfully and directly employed as supercapacitor electrodes, and they exhibited predominant electrochemical performances, such as a high $C_{sp}$ value of 1144 F $g^{-1}$ at 5 mV $s^{-1}$ and long-term cyclability. The excellent capacitive behaviors of $Co_3O_4/Ni(OH)_2$ composite mesoporous NNs grown on conductive substrate can be attributed to the following five factors: (i) the porous network structures that can accelerate the diffusion of active species, (ii) the mesopores within nanosheets that can favor proton transfer and provide a large $OH^-$ and cation accessible area, (iii) the interconnections among nanosheets that can facilitate electron transportation, (iv) the combination of cobalt and nickel anions that afford binary redox couples of $Co^{2+}/Co^{3+}$ and $Ni^{2+}/Ni^{3+}$, and (v) the direct growth on the current collector in a good solid contact that can greatly enhance the conductivity. Considering the simplicity of the electrodeposition method and environmentally friendly materials, the prepared $Co_3O_4/Ni(OH)_2$ composite mesoporous NNs as electrode is an competitive candidate for next generation supercapacitors owing to its outstanding electrochemical properties.

## Acknowledgements

This work was supported by NSFC (21073240, 51173212, and 90923008), Guangdong Province (2008B010600040 and 9251027501000002), and the Fundamental Research Funds for the Central Universities (11lgzd14).

## References

1 (*a*) D.-W. Wang, F. Li, J. Zhao, W. Ren, Z.-G. Chen, J. Tan, Z.-S. Wu, I. Gentle, G. Q. Lu and H.-M. Cheng, *ACS Nano*, 2009, **3**, 1745–1752; (*b*) S. Chen, J. Zhu and X. Wang, *J. Phys. Chem. C*, 2010, **114**, 11829–11834; (*c*) C. Liu, F. Li, L.-P. Ma and H.-M. Cheng, *Adv. Mater.*, 2010, **22**, E28–E62; (*d*) M. Heon, S. Lofland, J. Applegate, R. Nolte, E. Cortes, J. D. Hettinger, P.-L. Taberna, P. Simon, P. Huang, M. Brunet and Y. Gogotsi, *Energy Environ. Sci.*, 2011, **4**, 135–138; (*e*) R. Liu, J. Duay and S. B. Lee, *Chem. Commun.*, 2011, **47**, 1384–1404.

2 (*a*) Q. Wu, Y. Xu, Z. Yao, A. Liu and G. Shi, *ACS Nano*, 2010, **4**, 1963–1970; (*b*) D. Ahn, I. Yoo, Y.-M. Koo, N. Shin, J. Kim and T. J. Shin, *J. Mater. Chem.*, 2011, **21**, 5282–5289; (*c*) S. W. Lee, B. M. Gallant, H. R. Byon, P. T. Hammond and Y. Shao-Horn, *Energy Environ. Sci.*, 2011, **4**, 1972–1985; (*d*) Z. Li, J. Wang, X. Liu, S. Liu, J. Ou and S. Yang, *J. Mater. Chem.*, 2011, **21**, 3397–3403; (*e*) Y. Sun, Q. Wu and G. Shi, *Energy Environ. Sci.*, 2011, **4**, 1113–1132.

3 (*a*) P. J. Hall, M. Mirzaeian, S. I. Fletcher, F. B. Sillars, A. J. R. Rennie, G. O. Shitta-Bey, G. Wilson, A. Cruden and R. Carter, *Energy Environ. Sci.*, 2010, **3**, 1238–1251; (*b*) Y. Hou, Y. Cheng, T. Hobson and J. Liu, *Nano Lett.*, 2010, **10**, 2727–2733; (*c*) L. Bao, J. Zang and X. Li, *Nano Lett.*, 2011, **11**, 1215–1220; (*d*) X. Zhao, B. M. Sánchez, P. J. Dobson and P. S. Grant, *Nanoscale*, 2011, **3**, 839–855.

4 (*a*) I. Jung, J. Choi and Y. Tak, *J. Mater. Chem.*, 2010, **20**, 6164–6169; (*b*) J.-H. Kim, K. Zhu, Y. Yan, C. L. Perkins and A. J. Frank, *Nano Lett.*, 2010, **10**, 4099–4104; (*c*) J. Liu, J. Essner and J. Li, *Chem. Mater.*, 2010, **22**, 5022–5030; (*d*) C. Peng, S. Zhang, X. Zhou and G. Z. Chen, *Energy Environ. Sci.*, 2010, **3**, 1499–1502; (*e*) P. C. Sherrell, J. Chen, J. M. Razal, I. P. Nevirkovets, C. Crean, G. G. Wallace and A. I. Minett, *Energy Environ. Sci.*, 2010, **3**, 1979–1984.

5 (*a*) T. Brezesinski, J. Wang, J. Polleux, B. Dunn and S. H. Tolbert, *J. Am. Chem. Soc.*, 2009, **131**, 1802–1809; (*b*) P.-C. Chen, G. Shen, Y. Shi, H. Chen and C. Zhou, *ACS Nano*, 2010, **4**, 4403–4411; (*c*) S. Chen, J. Zhu, X. Wu, Q. Han and X. Wang, *ACS Nano*, 2010, **4**, 2822–2830; (*d*) H. Jiang, T. Zhao, C. Yan, J. Ma and C. Li, *Nanoscale*, 2010, **2**, 2195–2198; (*e*) A. J. Roberts and R. C. T. Slade, *J. Mater. Chem.*, 2010, **20**, 3221–3226.

6 (*a*) M. B. Sassin, A. N. Mansour, K. A. Pettigrew, D. R. Rolison and J. W. Long, *ACS Nano*, 2010, **4**, 4505–4514; (*b*) H.-Q. Wang, Z.-S. Li, Y.-G. Huang, Q.-Y. Li and X.-Y. Wang, *J. Mater. Chem.*, 2010, **20**, 3883–3889; (*c*) T.-Y. Wei, C.-H. Chen, H.-C. Chien, S.-Y. Lu and C.-C. Hu, *Adv. Mater.*, 2010, **22**, 347–351; (*d*) K.-H. Chang, C.-C. Hu, C.-M. Huang, Y.-L. Liu and C.-I. Chang, *J. Power Sources*, 2011, **196**, 2387–2392; (*e*) W. Shi, J. Zhu, D. H. Sim, Y. Y. Tay, Z. Lu, X. Zhang, Y. Sharma, M. Srinivasan, H. Zhang, H. H. Hng and Q. Yan, *J. Mater. Chem.*, 2011, **21**, 3422–3427.

7 (*a*) K. Brezesinski, J. Wang, J. Haetge, C. Reitz, S. O. Steinmueller, S. H. Tolbert, B. M. Smarsly, B. Dunn and T. Brezesinski, *J. Am. Chem. Soc.*, 2010, **132**, 6982–6990; (*b*) Y. Liang, M. G. Schwab, L. Zhi, E. Mugnaioli, U. Kolb, X. Feng and K. Müllen, *J. Am. Chem. Soc.*, 2010, **132**, 15030–15037; (*c*) R. Liu, J. Duay, T. Lane and S. Bok Lee, *Phys. Chem. Chem. Phys.*, 2010, **12**, 4309–4316; (*d*) H. Jiang, T. Zhao, J. Ma, C. Yan and C. Li, *Chem. Commun.*, 2011, **47**, 1264–1266.

8 (*a*) R. Liu and S. B. Lee, *J. Am. Chem. Soc.*, 2008, **130**, 2942–2943; (*b*) G. Wee, H. Z. Soh, Y. L. Cheah, S. G. Mhaisalkar and M. Srinivasan, *J. Mater. Chem.*, 2010, **20**, 6720–6725; (*c*) B. Li, H. Cao, J. Shao, M. Qu and J. H. Warner, *J. Mater. Chem.*, 2011, **21**, 5069–5075; (*d*) M. Salari, S. H. Aboutalebi, K. Konstantinov and H. K. Liu, *Phys. Chem. Chem. Phys.*, 2011, **13**, 5038–5041; (*e*) W. Wei, X. Cui, W. Chen and D. G. Ivey, *Chem. Soc. Rev.*, 2011, **40**, 1697–1721.

9 (*a*) C.-C. Hu, K.-H. Chang, M.-C. Lin and Y.-T. Wu, *Nano Lett.*, 2006, **6**, 2690–2695; (*b*) C.-C. Hu, Y.-L. Yang and T.-C. Lee, *Electrochem. Solid-State Lett.*, 2010, **13**, A173–A176.

10 (*a*) L. Cao, L.-B. Kong, Y.-Y. Liang and H.-L. Li, *Chem. Commun.*, 2004, 1646–1647; (*b*) T.-Y. Wei, C.-H. Chen, K.-H. Chang, S.-Y. Lu and C.-C. Hu, *Chem. Mater.*, 2009, **21**, 3228–3233.

11 Y. Lu, Y. Wang, Y. Zou, Z. Jiao, B. Zhao, Y. He and M. Wu, *Electrochem. Commun.*, 2010, **12**, 101–105.

12 C. Nethravathi, S. Sen, N. Ravishankar, M. Rajamathi, C. Pietzonka and B. Harbrecht, *J. Phys. Chem. B*, 2005, **109**, 11468–11472.

13 Y. Li, P. Hasin and Y. Wu, *Adv. Mater.*, 2010, **22**, 1926–1929.

14 C. C. Li, X. M. Yin, T. H. Wang and H. C. Zeng, *Chem. Mater.*, 2009, **21**, 4984–4992.

15 (*a*) C.-C. Hu, K.-H. Chang and C.-C. Wang, *Electrochim. Acta*, 2007, **52**, 4411–4418; (*b*) C.-C. Hu, H.-Y. Guo, K.-H. Chang and C.-C. Huang, *Electrochem. Commun.*, 2009, **11**, 1631–1634; (*c*) T. E. Quickel, V. H. Le, T. Brezesinski and S. H. Tolbert, *Nano Lett.*, 2010, **10**, 2982–2988.

16 (*a*) M. Oshitani, H. Yufu, K. Takashima, S. Tsuji and Y. Matsumaru, *J. Electrochem. Soc.*, 1989, **136**, 1590–1593; (*b*) J. Chen, D. H. Bradhurst, S. X. Dou and H. K. Liu, *J. Electrochem. Soc.*, 1999, **146**, 3606–3612.

17 H. Jin, T. Okamoto and M. Ishida, *Energy Fuels*, 1998, **12**, 1272–1277.

18 (*a*) J. Baxter, Z. Bian, G. Chen, D. Danielson, M. S. Dresselhaus, A. G. Fedorov, T. S. Fisher, C. W. Jones, E. Maginn, U. Kortshagen, A. Manthiram, A. Nozik, D. R. Rolison, T. Sands, L. Shi, D. Sholl and Y. Wu, *Energy Environ. Sci.*, 2009, **2**, 559–588; (*b*) H. Wang, H. S. Casalongue, Y. Liang and H. Dai, *J. Am. Chem. Soc.*, 2010, **132**, 7472–7477; (*c*) F. B. Sillars, S. I. Fletcher, M. Mirzaeian and P. J. Hall, *Energy Environ. Sci.*, 2011, **4**, 695–706.

19 (*a*) Q. Qu, P. Zhang, B. Wang, Y. Chen, S. Tian, Y. Wu and R. Holze, *J. Phys. Chem. C*, 2009, **113**, 14020–14027; (*b*) L. Zheng, Y. Xu, D. Jin and Y. Xie, *J. Mater. Chem.*, 2010, **20**, 7135–7143; (*c*) S. Xiong, C. Yuan, X. Zhang and Y. Qian, *CrystEngComm*, 2011, **13**, 626–632.

20 (*a*) C. Xu, Y. Zhao, G. Yang, F. Li and H. Li, *Chem. Commun.*, 2009, 7575–7577; (*b*) R. Liu, J. Duay and S. B. Lee, *ACS Nano*, 2010, **4**, 4299–4307; (*c*) Z.-S. Wu, W. Ren, D.-W. Wang, F. Li, B. Liu and H.-M. Cheng, *ACS Nano*, 2010, **4**, 5835–5842; (*d*) J. Yan, E. Khoo, A. Sumboja and P. S. Lee, *ACS Nano*, 2010, **4**, 4247–4255.

21 (*a*) L. Ran, *et al.*, *Nanotechnology*, 2008, **19**, 215710; (*b*) Z. Niu, W. Zhou, J. Chen, G. Feng, H. Li, W. Ma, J. Li, H. Dong, Y. Ren, D. Zhao and S. Xie, *Energy Environ. Sci.*, 2011, **4**, 1440–1446; (*c*) M. Salari, K. Konstantinov and H. K. Liu, *J. Mater. Chem.*, 2011, **21**, 5128–5133.

22 (*a*) A. V. Murugan, T. Muraliganth and A. Manthiram, *Chem. Mater.*, 2009, **21**, 5004–5006; (*b*) L. Wang, D. Wang, X. Y. Dong, Z. J. Zhang, X. F. Pei, X. J. Chen, B. Chen and J. Jin, *Chem. Commun.*, 2011, **47**, 3556–3558; (*c*) L. Wei, C. Li, H. Chu and Y. Li, *Dalton Trans.*, 2011, **40**, 2332–2337; (*d*) M. A. Woo, M.-S. Song, T. W. Kim, I. Y. Kim, J.-Y. Ju, Y. S. Lee, S. J. Kim, J.-H. Choy and S.-J. Hwang, *J. Mater. Chem.*, 2011, **21**, 4286–4292.

23 (*a*) T. Brezesinski, J. Wang, R. Senter, K. Brezesinski, B. Dunn and S. H. Tolbert, *ACS Nano*, 2010, **4**, 967–977; (*b*) T. Brezesinski, J. Wang, S. H. Tolbert and B. Dunn, *Nat. Mater.*, 2010, **9**, 146–151; (*c*) F. Su, C. K. Poh, J. S. Chen, G. Xu, D. Wang, Q. Li, J. Lin and X. W. Lou, *Energy Environ. Sci.*, 2011, **4**, 717–724; (*d*) S. Yoon, E. Kang, J. K. Kim, C. W. Lee and J. Lee, *Chem. Commun.*, 2011, **47**, 1021–1023.

24 (*a*) C. Yuan, X. Zhang, L. Su, B. Gao and L. Shen, *J. Mater. Chem.*, 2009, **19**, 5772–5777; (*b*) T. Zhu, J. S. Chen and X. W. Lou, *J. Mater. Chem.*, 2010, **20**, 7015–7020; (*c*) X.-H. Xia, J.-P. Tu, X.-L. Wang, C.-D. Gu and X.-B. Zhao, *J. Mater. Chem.*, 2011, **21**, 671–679.

25 (*a*) J.-K. Chang, C.-M. Wu and I. W. Sun, *J. Mater. Chem.*, 2010, **20**, 3729–3735; (*b*) M.-S. Wu and M.-J. Wang, *Chem. Commun.*, 2010, **46**, 6968–6970; (*c*) C.-Y. Cao, W. Guo, Z.-M. Cui, W.-G. Song and W. Cai, *J. Mater. Chem.*, 2011, **21**, 3204–3209; (*d*) H. Jiang, T. Zhao, C. Li and J. Ma, *J. Mater. Chem.*, 2011, **21**, 3818–3823; (*e*) J. Liu, C. Cheng, W. Zhou, H. Li and H. J. Fan, *Chem. Commun.*, 2011, **47**, 3436–3438; (*f*) S. K. Meher, P. Justin and G. Ranga Rao, *Nanoscale*, 2011, **3**, 683–692; (*g*) C. Xu, J. Sun and L. Gao, *CrystEngComm*, 2011, **13**, 1586–1590.

26 (*a*) K. Nakaoka, M. Nakayama and K. Ogura, *J. Electrochem. Soc.*, 2002, **149**, C159–C163; (*b*) A. Bai and C.-C. Hu, *Electrochem. Commun.*, 2003, **5**, 78–82; (*c*) A. Bai and C.-C. Hu, *Electrochem. Commun.*, 2003, **5**, 619–624; (*d*) K. R. Prasad and N. Miura, *Appl. Phys. Lett.*, 2004, **85**, 4199–4201; (*e*) J.-S. Do and R.-F. Dai, *J. Power Sources*, 2009, **189**, 204–210; (*f*) M.-J. Deng, F.-L. Huang, I.-W. Sun, W.-T. Tsai and J.-K. Chang, *Nanotechnology*, 2009, **20**, 175602.

27 P. Poizot, S. Laruelle, S. Grugeon, L. Dupont and J. M. Tarascon, *Nature*, 2000, **407**, 496–499.

28 Z.-S. Wu, W. Ren, L. Wen, L. Gao, J. Zhao, Z. Chen, G. Zhou, F. Li and H.-M. Cheng, *ACS Nano*, 2010, **4**, 3187–3194.

29 Y. Li, B. Tan and Y. Wu, *Nano Lett.*, 2007, **8**, 265–270.

30 J. Jiang, J. Liu, R. Ding, X. Ji, Y. Hu, X. Li, A. Hu, F. Wu, Z. Zhu and X. Huang, *J. Phys. Chem. C*, 2009, **114**, 929–932.

31 Y. Wang, H. Xia, L. Lu and J. Lin, *ACS Nano*, 2010, **4**, 1425–1432.

32 W. Li, S. Zhang and J. Chen, *J. Phys. Chem. B*, 2005, **109**, 14025–14032.

33 Z. P. Xu and H. C. Zeng, *Chem. Mater.*, 1998, **11**, 67–74.

34 Y. Zhu, H. Li, Y. Koltypin and A. Gedanken, *J. Mater. Chem.*, 2002, **12**, 729–733.

35 Z. Liu, R. Ma, M. Osada, K. Takada and T. Sasaki, *J. Am. Chem. Soc.*, 2005, **127**, 13869–13874.

36 P. V. Kamath, G. H. Annal Therese and J. Gopalakrishnan, *J. Solid State Chem.*, 1997, **128**, 38–41.

37 X. H. Huang, J. P. Tu, X. H. Xia, X. L. Wang, J. Y. Xiang, L. Zhang and Y. Zhou, *J. Power Sources*, 2009, **188**, 588–591.

38 B. Ash, R. K. Paramguru and B. K. Mishra, *Electrochem. Commun.*, 2010, **12**, 48–51.

39 C.-C. Hu, C.-C. Huang and K.-H. Chang, *Electrochem. Commun.*, 2009, **11**, 434–437.

40 C.-C. Huang, H.-C. Hsu, C.-C. Hu, K.-H. Chang and Y.-F. Lee, *Electrochim. Acta*, 2010, **55**, 7028–7035.

41 X. Wang, F. Zhang, X. Zhu, B. Xia, J. Chen, S. Qiu and J. Li, *J. Colloid Interface Sci.*, 2009, **337**, 272–277.

42 L.-Z. Fan and J. Maier, *Electrochem. Commun.*, 2006, **8**, 937–940.

43 H. Mi, X. Zhang, X. Ye and S. Yang, *J. Power Sources*, 2008, **176**, 403–409.

44 A. Gaunand and W. L. Lim, *Powder Technol.*, 2002, **128**, 332–337.

45 P. Oliva, J. Leonardi, J. F. Laurent, C. Delmas, J. J. Braconnier, M. Figlarz, F. Fievet and A. d. Guibert, *J. Power Sources*, 1982, **8**, 229–255.

46 Y. Xu, Q. Feng, K. Kajiyoshi, K. Yanagisawa, X. Yang, Y. Makita, S. Kasaishi and K. Ooi, *Chem. Mater.*, 2002, **14**, 3844–3851.

47 Z.-A. Hu, Y.-L. Xie, Y.-X. Wang, L.-J. Xie, G.-R. Fu, X.-Q. Jin, Z.-Y. Zhang, Y.-Y. Yang and H.-Y. Wu, *J. Phys. Chem. C*, 2009, **113**, 12502–12508.

48 H. Pang, Q. Lu, Y. Li and F. Gao, *Chem. Commun.*, 2009, 7542–7544.


 

49 Y. E. Roginskaya, O. V. Morozova, E. N. Lubnin, Y. E. Ulitina, G. V. Lopukhova and S. Trasatti, *Langmuir*, 1997, **13**, 4621–4627.
50 J. G. Kim, D. L. Pugmire, D. Battaglia and M. A. Langell, *Appl. Surf. Sci.*, 2000, **165**, 70–84.
51 M. M. Natile and A. Glisenti, *Chem. Mater.*, 2002, **14**, 3090–3099.
52 G. B. Hoflund and W. S. Epling, *Chem. Mater.*, 1998, **10**, 50–58.
53 M. M. Natile and A. Glisenti, *Chem. Mater.*, 2002, **14**, 4895–4903.
54 S. Deki, A. Hosokawa, A. B. Béléké and M. Mizuhata, *Thin Solid Films*, 2009, **517**, 1546–1554.
55 M. M. Natile and A. Glisenti, *Chem. Mater.*, 2003, **15**, 2502–2510.
56 J. F. Marco, J. R. Gancedo, M. Gracia, J. L. Gautier, E. Ríos and F. J. Berry, *J. Solid State Chem.*, 2000, **153**, 74–81.
57 S. R. Shieh and T. S. Duffy, *Phys. Rev. B: Condens. Matter*, 2002, **66**, 134301.
58 W. Wang, Y. Liu, C. Xu, C. Zheng and G. Wang, *Chem. Phys. Lett.*, 2002, **362**, 119–122.
59 T. Yu, Y. W. Zhu, X. J. Xu, Z. X. Shen, P. Chen, C. T. Lim, J. T. L. Thong and C. H. Sow, *Adv. Mater.*, 2005, **17**, 1595–1599.
60 Y. Li, B. Tan and Y. Wu, *J. Am. Chem. Soc.*, 2006, **128**, 14258–14259.
61 W. G. Pell and B. E. Conway, *J. Power Sources*, 2001, **96**, 57–67.
62 C.-C. Hu, K.-H. Chang and T.-Y. Hsu, *J. Electrochem. Soc.*, 2008, **155**, F196–F200.
63 H. Chen, J. M. Wang, T. Pan, H. M. Xiao, J. Q. Zhang and C. N. Cao, *Int. J. Hydrogen Energy*, 2003, **28**, 119–124.
64 K. Watanabe, T. Kikuoka and N. Kumagai, *J. Appl. Electrochem.*, 1995, **25**, 219–226.
65 L. Chen, L. Li and G. Li, *J. Solid State Chem.*, 2008, **181**, 2073–2077.
66 Y.-T. Wu and C.-C. Hu, *J. Electrochem. Soc.*, 2004, **151**, A2060–A2066.